High-resolution and quantitative spatial analysis reveal intra-ductal phenotypic and functional diversification in pancreatic cancer

Michiels, E.; Madhloum, H.; Lint, S. van; Messaoudi, N.; Kunda, R.; Martens, S.; ... ; Rooman, I.

Journal of Pathology
J Pathol January 2024; **262:** 76–89
Published online 16 October 2023 in Wiley Online Library
(wileyonlinelibrary.com) DOI: 10.1002/path.6212

ORIGINAL ARTICLE

High-resolution and quantitative spatial analysis reveal intra-ductal phenotypic and functional diversification in pancreatic cancer

Ellis Michiels[1], Hediel Madhloum[1†], Silke Van Lint[1†], Nouredin Messaoudi[2], Rastislav Kunda[2], Sandrina Martens[1,3], Philippe Giron[4], Catharina Olsen[4], Pierre Lefesvre[5], Nelson Dusetti[6], Leila EL Mohajer[6], Richard Tomasini[6], Lukas JAC Hawinkels[7], Farah Ahsayni[2], Rémy Nicolle[8], Tatjana Arsenijevic[9,10], Christelle Bouchart[11], Jean-Luc Van Laethem[9,10] and Ilse Rooman[1*]

[1] *Laboratory of Medical & Molecular Oncology (LMMO), Vrije Universiteit Brussel (VUB), Brussels, Belgium*
[2] *Department of Surgery, Department of Gastroenterology-Hepatology, Department of Advanced Interventional Endoscopy, Universitair Ziekenhuis Brussel (UZB), Vrije Universiteit Brussel (VUB), Brussels, Belgium*
[3] *Department of Cardio and Organ Systems, Biomedical Research Institute, Hasselt University, Diepenbeek, Belgium*
[4] *Centre for Medical Genetics, Clinical Sciences, Reproduction and Genetics Research Group, Universitair Ziekenhuis Brussel (UZB), Vrije Universiteit Brussel (VUB), Brussels, Belgium*
[5] *Department of Anatomo-Pathology, Universitair Ziekenhuis Brussel (UZB), Brussels, Belgium*
[6] *Cancer Research Center of Marseille (CRCM), INSERM, CNRS, Institut Paoli-Calmettes, Aix-Marseille, Marseille University, Marseille, France*
[7] *Department of Gastroenterology and Hepatology, Leiden University Medical Center (LUMC), Leiden, The Netherlands*
[8] *Centre de Recherche sur l'inflammation (CRI), INSERM, Paris, France*
[9] *Laboratory of Experimental Gastroenterology, Faculty of Medicine, Université Libre de Bruxelles (ULB), Bruxelles, Belgium*
[10] *Department of Gastroenterology, Hepatology and Digestive Oncology, HUB Bordet Erasme Hospital, Université Libre de Bruxelles, Brussels, Belgium*
[11] *Department of Radiation-Oncology, Université Libre de Bruxelles (ULB), Hospital Universitaire de Bruxelles (HUB) Institut Jules Bordet, Brussels, Belgium*

**Correspondence to: I Rooman, Vrije Universiteit Brussel, Laarbeeklaan 103, 1090 Jette, Brussels, Belgium. E-mail: ilse.rooman@vub.be*

[†]Equal contibutions.

Abstract

A 'classical' and a 'basal-like' subtype of pancreatic cancer have been reported, with differential expression of *GATA6* and different dosages of mutant *KRAS*. We established *in situ* detection of *KRAS* point mutations and mRNA panels for the consensus subtypes aiming to project these findings to paraffin-embedded clinical tumour samples for spatial quantitative analysis. We unveiled that, next to inter-patient and intra-patient inter-ductal heterogeneity, intraductal spatial phenotypes exist with anti-correlating expression levels of *GATA6* and $KRAS^{G12D}$. The basal-like mRNA panel better captured the basal-like cell states than widely used protein markers. The panels corroborated the co-existence of the classical and basal-like cell states in a single tumour duct with functional diversification, i.e. proliferation and epithelial-to-mesenchymal transition respectively. Mutant $KRAS^{G12D}$ detection ascertained an epithelial origin of vimentin-positive cells in the tumour. Uneven spatial distribution of cancer-associated fibroblasts could recreate similar intra-organoid diversification. This extensive heterogeneity with functional cooperation of plastic tumour cells poses extra challenges to therapeutic approaches.

Keywords: molecular heterogeneity; mutation detection; spatial subtyping; pancreatic cancer; plasticity

Received 11 April 2023; Revised 23 August 2023; Accepted 2 September 2023

No conflicts of interest were declared.

Introduction

Pancreatic ductal adenocarcinoma (PDAC) is the most common pancreatic cancer and is known for its extremely aggressive behaviour, resulting in a high mortality rate and a 5-year survival of only 11% [1]. In the last decade, several next-generation sequencing (NGS)-based studies have identified two major transcriptomic subtypes, termed classical and basal-like [2–6]. The classical subtype is characterised by well-differentiated epithelial duct-like structures and is associated with a better prognosis [5]. A typical gene signature of classical PDAC includes expression of pancreatic precursor genes and genes involved in lipogenesis and cholesterol metabolism [7]. Basal-like tumours have a poorer prognosis [8] and are frequently associated with metastasis [9]. Basal-like

tumour cells are less differentiated [5] and express genes related to epithelial-to-mesenchymal transition (EMT), hypoxia [9], and chemoresistance [10]. The expression of GATA6 – a transcription factor whose primary function is epithelial differentiation – is increased in classical tumours and represents a prognostically valuable marker to distinguish both subtypes [11,12]. Nevertheless, recent transcriptomic findings from bulk or single-cell studies revealed the coexistence of classical and basal-like regions within a single tumour [13] and the presence of an intermediate cell state with co-expression of classical and basal-like features [14]. This phenotypic heterogeneity in human PDAC should be better captured and understood when studying tumour biology, performing diagnostics, or evaluating drug response.

Mutant *KRAS* is the most prevalent oncogenic driver in human PDAC and has prognostic value in the clinic [15]. While some papers describe RAS independence in basal-like tumour cells, others report the highest mutation levels of *KRAS* in most undifferentiated basal-like tumours and show that oncogenic dosage variation is associated with tumour aggressiveness, metastatic potential, and poorer response to therapy [6,10,14,36]. These seemingly contradictory results suggest that the expression of *KRAS* could be non-genetically regulated and that transcriptional determination of tumour cell state may be influenced by the microenvironment [14].

All PDAC subtyping studies were based on transcriptomic analysis of bulk tissue, where in most cases tumour and stroma were separated physically or digitally. Although this has led to the two-classification system for PDAC, such profiling efforts do not allow for the quantitative study of tumour heterogeneity in a morphological, histological, and, thus, spatial context. Therefore, we have successfully optimised RNA *in situ* hybridisation techniques to spatially detect $KRAS^{G12D}$ (the most common point mutation) along with *GATA6* transcripts on paraffin sections of human PDAC and organoids [16–18]. This *in situ* approach showed phenotypic diversification down to the level of a single duct in a tumour. We comprehensively phenotyped the tissue at single-cell resolution using subtype-specific mRNA panels that were directly informed by the bulk sequencing studies, confirming extensive intra-ductal heterogeneity, which further extends to functional diversification. These techniques and the insights gained from them call for robust spatial analysis informing diagnostic and therapeutic strategies.

Materials and methods

See Supplementary materials and methods for additional details.

Human samples

Surgical resections were obtained from patients at the Gastroenterology Department of UZ Brussels, Belgium. Informed consent was obtained from all patients included in the study. The use of clinical samples and data conformed with the national guidelines and regulations in Belgium (UZ Brussel, B.U.N. 143201941917).

RNA *in situ* hybridisation (ISH) using RNAScope™

Manual RNAScope™ was performed on formalin-fixed, paraffin-embedded (FFPE) tissue sections in accordance with the manufacturer's guidelines using the Multiplex Fluo Reagent Kit version 2 (ACD, Newark, CA, USA, no. 323100). In brief, after pretreatment with heat and proteases, slides were incubated with RNAScope™ probes for *GATA6* (supplementary material, Table S2) overnight in a HybEZ oven (ACD). Signal was enhanced using amplifier molecules and detected with fluorophores diluted in TSA buffer (ACD, no. 322809). After a protein block with casein, primary antibodies were applied overnight, and sections were further processed as described in Supplementary materials and methods. For automated multiplex RNAScope™, FFPE sections were dried overnight at 40 °C and kept at 4 °C. RNAscope™ LS 4-plex Fluorescent Assay (ACD) was run on the Leica Bond RX (Leica Biosystems, Buffalo Grove, IL, USA) (target retrieval: 15 min, ER2 at 95 °C, followed by 15 min with Protease III). Controls included RNAscope™ 2.5 LS Multiplex Positive Control Probe kit (*POLR2A*, *PPIB*, *UBC*, and *HPRT-1*) and RNAscope™ 2.5 LS 4-plex Negative Control Probe (*DapB*, *Bacillus subtilis*) (supplementary material, Table S1).

RNA *in situ* hybridisation (BaseScope™)

The BaseScope™ assay started with cutting FFPE tissue freshly under RNAse-free conditions. The day after, the BaseScope™ RED v2 kit (ACD, no. 323600) was run on the Leica Bond RX™ (heat = 15 min) and protease III (88 °C, 15 min), followed by hybridisation with BaseScope™-specific 1zz probe pairs (supplementary material, Table S1). A series of amplification reagents enhanced the signal, then alkaline phosphatase-labelled probes were hybridised and detected using the RED chromogenic substrate.

Immunofluorescence

Paraffin sections were baked, deparaffinised in toluene, and rehydrated in propanol. To block endogenous peroxidase activity, sections were immersed in 3% hydrogen peroxide in methanol (30 min, RT). Antigen retrieval was carried out in citrate buffer (Sigma-Aldrich, St-Louis, MO, USA, no. C9999) in a pressure cooker for 40 min. Slides were incubated with protein block for 30 min using 25% diluted casein (Thermo Fisher Scientific, Waltham, MA, USA, no. 37528). Primary antibodies (supplementary material, Table S2) were incubated overnight at 4 °C. Next, a cocktail of fluorescent-labelled secondary antibodies was applied on the sections (supplementary material, Table S2) together with a Hoechst dye (Thermo Fisher Scientific, no. H1399, diluted 1/250) for detection of nuclei. Slides were mounted using ProLong Gold Antifade mounting medium (Thermo Fisher

Scientific, no. P36930). We replaced primaries one by one with BOND Antibody Diluent (Leica Biosystems) as negative controls. In addition, we replaced the mix of primary antibodies (maximum 3) with BOND Antibody Diluent to look for any interaction between secondary antibodies.

Statistics

GraphPad Prism version 8.0 software was used (GraphPad Inc., San Diego, CA, USA. Single-cell count data were analysed using a signed-ranked Wilcoxon test (paired data) and Mann–Whitney test (unpaired data). We used the Log-Rank (Mantel-Cox) test for generating Kaplan–Meier curves. For multiregion analysis, we performed two-way ANOVA for repeated measures. We applied Spearman correlation to determine spatial correlations. Figure legends show the number of independent experiments (N), and results are shown as median with interquartile range, because we used non-parametric statistical tests. Significance was accepted when $p < 0.05$.

Results

High-resolution *in situ* analysis of *GATA6* reveals inter-patient, intra-patient inter-ductal, and intra-ductal heterogeneity

As *GATA6* is generally used as a transcriptomic study-derived biomarker to distinguish between classical and basal-like PDAC, we examined *GATA6* mRNA expression using RNAScope™ in a cohort of PDAC resections ($N = 20$, Figure 1A and supplementary material, Table S3). *GATA6* was found to be distributed heterogenously, with spatial plots showing samples with predominantly high and others with predominantly low ISH scores (supplementary material, Figures SA1A–D and S2, and Table S4). We divided the cohort into two groups, with the median value of *GATA6* transcripts measured per cell as the cut-off (*GATA6*^{high} and *GATA6*^{low}, Figure 1A). The *GATA6*^{high} group expresses an average of 3.5 dots/cell, while the *GATA6*^{low} samples have 1.9 dots/cell (supplementary material, Figure S1E). The RNAScope™ H-scores were 108 and 79 respectively (supplementary material, Figure S1F). Compared with *GATA6*^{high} tumours, *GATA6*^{low} tumours were enriched in grade 3 or 4 tumours (0% versus 36%) and are more frequently associated with lymph node invasion (33% versus 72%) and tumour recurrence (33% versus 54%). The mean overall survival (OS) time of all patients was 17 months (supplementary material, Table S5). The 2-year survival rate after surgery was lower for *GATA6*^{low} tumours (89% versus 54%). Of note, the cause of the only death we observed in the *GATA6*^{high} group was not cancer related. *KRAS* point mutations were identified by NGS and/or Idylla analysis and were, together with *TP53* mutations, most prevalent (Figure 1A and supplementary material, Figure S1J). Regarding transcriptomic subtypes, most quasi-mesenchymal (Collisson), squamous (Bailey), stroma-activated (Puleo), pure-basal (Puleo), and basal B (Chan-Seng-Yue) signatures overlap with the *GATA6*^{low} population, whereas the classical (Collisson), pancreatic progenitor (Bailey), pure-classical (Puleo), and classical A (Chan-Seng-Yue) samples belong to the *GATA6*^{high} population [2,4–6] (Figure 1A).

To comprehensively investigate intra-patient heterogeneity, we first defined a single tumour duct-like structure ('tumour duct') where an irregularly shaped lumen is surrounded by a multilayer of PanCK^{+} cells organised as a cylindrical epithelium and morphologically characterised by larger nuclei, reduced cytoplasm, and loss of polarity. We measured *GATA6* ISH scores (Supplementary materials and methods and supplementary material, Figure S1I and Table S4) and observed heterogenous expression of *GATA6* between ducts (Figure 1B,D,F and supplementary material, Figures S1G, S3A,B) and within different regions of a single tumour duct (Figures 1C,E,G and supplementary material, Figure S1H). *GATA6* ISH scores correlate with GATA6 antibody stainings (not shown). Ductal tumour cells had *GATA6* ISH scores ranging from 0 to 4 (supplementary material, Table S3) when assessing multiple ducts per patient (Figure 1F and supplementary material, Figures S1I, S3A,B) and when assessing multiple ROIs per duct (Figure 1G and supplementary material, Figure S1H). We identified PDAC077 (grey bullet) as the least heterogenous (dotted line in Figure 1F,G). These data demonstrate that intra-patient heterogeneity for expression of *GATA6* extends to different regions in a single tumour duct.

Optimisation of a BaseScope™ assay for high-resolution *in situ* analysis of *KRAS*^{G12D}

We optimised the BaseScope™ assay to detect and measure point mutations in FFPE sections of PDAC (Figure 2A), as increased *KRAS* dosage was reported in the most aggressive (basal-like) tumours [10].

BaseScope™ in combination with immunostaining for PanCK was successful after adjustments (see Materials and methods) to the manufacturer's protocol (ACD). In the homozygous *KRAS*^{G12D} mutant cell line (SW1990), the *KRAS*^{G12D} probe stained ~40% of the cells while the *KRAS* wild-type cell line (BxPC3) showed nonspecific *KRAS*^{G12D} signal in ≤2% of cells, which was equivalent to the non-specific signals using a negative control probe (bacterial *DapB*). In line with this, using the *KRAS*^{WT} probe we detected a positive signal in ~60% of BxPC3 cells and a background signal of ≤2% in SW1990 (supplementary material, Figure S4A). In the heterozygous *KRAS*^{G12V} mutant cell line (PaTu8889T), *KRAS*^{G12V} was detected in 22% of tumour cells, while <1% were false positive for *DapB* (supplementary material, Figure S4B). In patient tissue (*KRAS*^{G12D} mutant by NGS and/or Idylla), an average of 24% of tumour cells stained positive for *KRAS*^{G12D} ($N = 6$, Figure 2B), and in the *KRAS*^{G12V} mutants, ~8% of tumour cells stained positive for *KRAS*^{G12V} ($N = 4$,

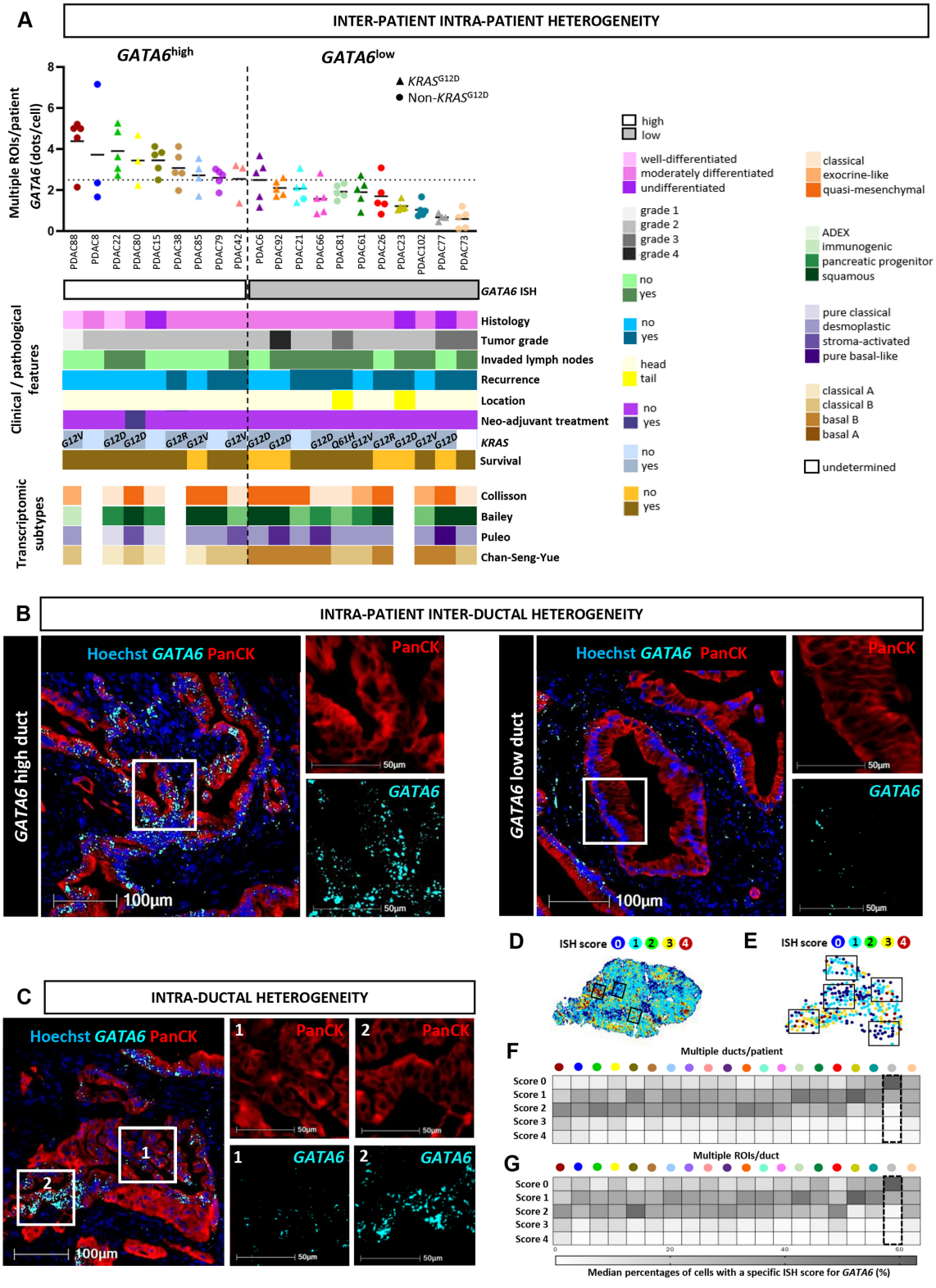

Figure 1. Inter-patient, intra-patient inter-ductal, and intra-ductal heterogeneity of *GATA6* expression. (A) Clinical, pathological, and transcriptomic characteristics of all PDAC patients ($N = 20$) divided into *GATA6*^{high} versus *GATA6*^{low} subgroups, according to *GATA6* ISH (RNAScope™), with the horizontal dotted line representing the median value. *KRAS* point mutations are determined with NGS and/or Idylla. (B and C) *GATA6* ISH combined with immunofluorescence (IF) for Pan-cytokeratin (PanCK) in representative *GATA6*^{high} and *GATA6*^{low} tumour ducts derived from a single patient (B) and in *GATA6*^{high} versus *GATA6*^{low} ductal regions present in a single tumour duct (C). Scale bars, 100 µm; insets, 50 µm. (D and E) Spatial plots of *GATA6* expression on single-cell level, with different colours representing ISH scores from 0 to 4, on whole-tissue section (D) and on a single tumour duct (E). The same patient's tissue is used as in panels B and C. (F–G) Heat maps to quantitatively represent inter-ductal (F) and intra-ductal heterogeneity (IDH) (G) of *GATA6* RNAScope™. Median percentages of cells with a specific ISH score are shown per patient ($N = 20$; three ducts/patient in F, three ROIs/duct in G). Following the criteria to define IDH (Supplementary materials and methods), we identify one sample without IDH (dotted lines). Colour annotation for individual patients as in Figure 1A, and supplementary material, Figures S2 and S3.

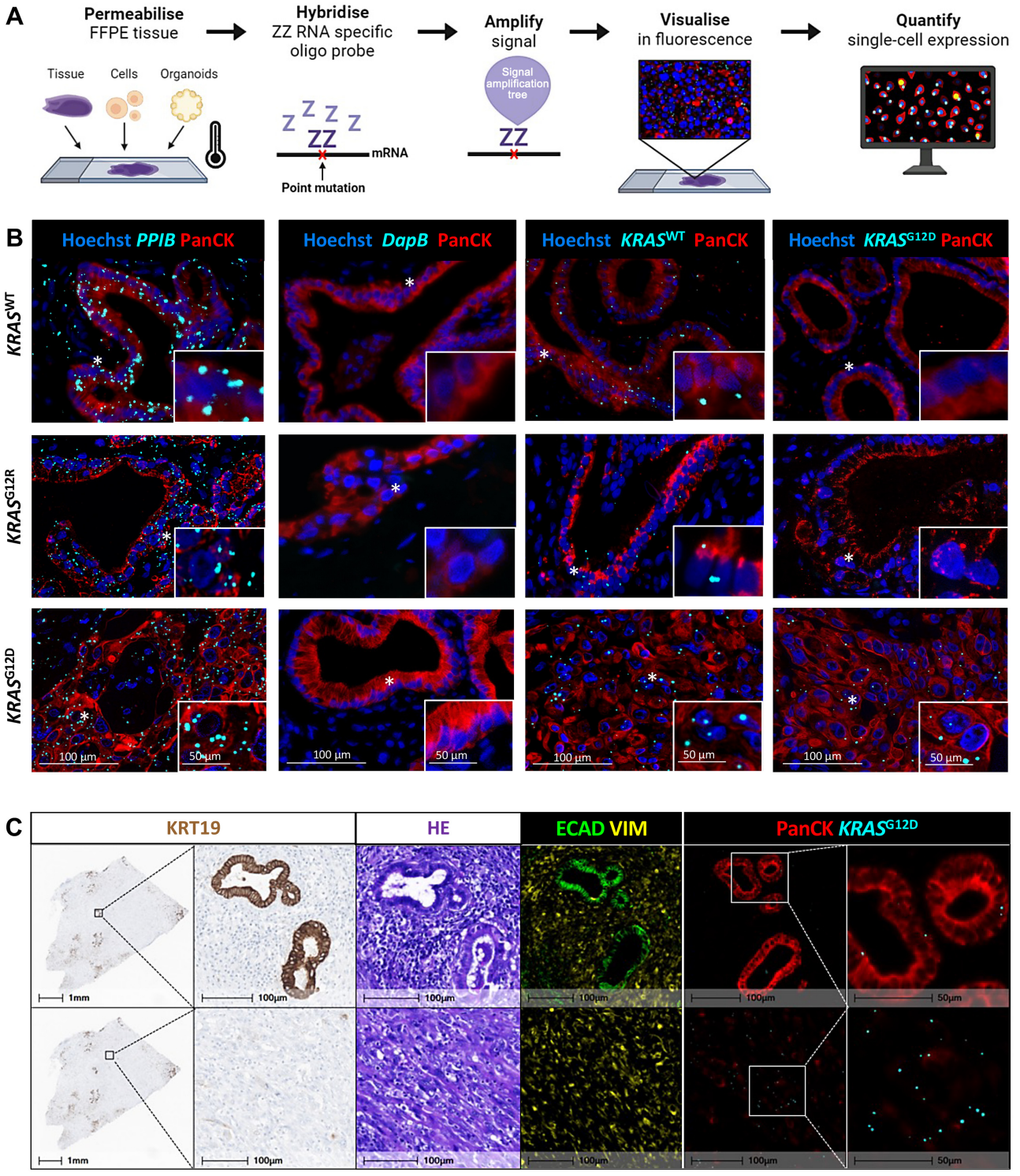

Figure 2. BaseScope™ assay for *in situ* detection of *KRAS*^{G12D} point mutation. (A) Graphical representation of BaseScope™ assay. The thermometer refers to heat-induced tissue permeabilisation. Created with BioRender.com. (B) BaseScope™ detection of *KRAS*^{WT} and *KRAS*^{G12D} transcripts on paraffin-embedded sections of human PDAC identified as *KRAS*^{WT}, *KRAS*^{G12R}, and *KRAS*^{G12D} with NGS and/or Idylla. *PPIB* and *DapB* are used as positive control (+ ctrl) and negative control (− ctrl) probes respectively. Tumour epithelial cells were stained with PanCK. Scale bars, 50 µm; insets, 20 µm. Source regions of insets are indicated by white asterisk. (C) Undifferentiated tumour cells that are hard to distinguish from stroma with haematoxylin-eosin (HE) or with immunostaining for cytokeratin 19 (KRT19) or vimentin are identified by the BaseScope™ assay being *KRAS*^{G12D} positive. Scale bars, 1 mm and 100 and 50 µm.

supplementary material, Figure S4B), again with <2% false positives (not shown). *KRAS*^{WT} was detected in ~30% of tumour cells in *KRAS*^{G12D}, *KRAS*^{G12R}, *and* *KRAS*^{G12V} samples, whereas *KRAS*^{G12D} was not detected in *KRAS*^{WT}, *KRAS*^{G12R}, or *KRAS*^{G12V} samples ($N = 7$; Figure 2B and supplementary material, Figure S4B). Of note, the BaseScope™ assay allowed us to distinguish undifferentiated vimentin-positive tumour cells

from host stromal cells, with which they could easily be confounded (Figure 2C).

In summary, we reliably detected the two most prevalent *KRAS* point mutations in FFPE clinical samples using an optimised BaseScope™ assay.

Spatial phenotypes of *GATA6* and *KRAS*^{G12D} expression underscore inter-patient, intra-patient inter-ductal, and intra-ductal heterogeneity

Spatial plots of a classical subtyped and a basal-like subtyped sample showed, respectively, overall high expression of *GATA6* and only a small proportion of cells positive for *KRAS*^{G12D} versus low *GATA6* ISH scores along with high positivity for *KRAS*^{G12D} (Figure 3A and supplementary material, Figure S5A). When we integrated the *KRAS*^{G12D} single-cell quantifications with the *GATA6*$^{high/low}$ groups from Figure 1, we could discriminate four tumour phenotypes, with *GATA6*^{high}/*KRAS*^{G12Dlow} and *GATA6*^{low}/*KRAS*^{G12Dhigh} as the extremes (black and white in the Figure 3B legend), that tend to have prognostic value (supplementary material, Figure S5D). Of 13 samples that were called to be non-G12D by NGS and/or Idylla, nine actually gave Basescope™ staining for *KRAS*^{G12D} above the threshold (red line in Figure 3B). This indicates that the BaseScope™ assay at the single-cell level is more sensitive than the bulk assays (NGS/Idylla).

To assess whether the tumour phenotypes also exist as 'spatial phenotypes' in an individual patient and to what extent, we used all NGS-confirmed *KRAS*^{G12D} samples ($N = 7$). As an illustration, ROI 1 had lower *GATA6* and higher *KRAS*^{G12D}, whereas ROI 2 was composed mainly of cells with high *GATA6* and decreased *KRAS*^{G12D} (Figure 3C,D and supplementary material, Figure S5B). Comparison of multiple ROIs per patient revealed a significant negative spatial correlation between *GATA6* and *KRAS*^{G12D} (Figure 3E). The spatial phenotypes varied in prevalence in various ducts of one patient (Figure 3F,G), with on average 42% of tumour cells that were *KRAS*^{G12Dlow}/*GATA6*^{high}. Notably, almost 50% were of an intermediate phenotype (*KRAS*^{G12Dlow}/*GATA6*^{low}, *KRAS*G12Dhigh/*GATA6*high). At the intra-ductal level (Figure 3H,I and supplementary material, Figure S5C), again, a negative correlation between *GATA6* and *KRAS*^{G12D} existed (Figure 3J), and on average 26% of tumour cells were *KRAS*^{G12Dlow}/*GATA6*^{high} and half had an intermediate phenotype (Figure 3K). Figure 3L demonstrates spatial variability between multiple ROIs in one tumour duct. Overall, a widespread heterogeneity exists down to the level of a single tumour duct with anti-correlating *KRAS*^{G12D} and *GATA6* and a substantial proportion of cells of an intermediate phenotype.

Intra-patient inter-ductal and intra-ductal spatial heterogeneity of a classical and basal-like marker panel

We extended our analysis using novel mRNA marker panels (multiplex RNAscope™) for the classical and basal-like subtypes, selecting markers directly informed by the bulk transcriptomic signatures reported by Bailey *et al* [4] and Puleo *et al* [5]. Differentially expressed genes in both studies were investigated for their biological significance in (pancreatic) cancer via a PubMed literature search. The classical gene panel (CP) consists of *GATA6*, *NR1I2*, *CTSE*, and *EPS8L3*, and the basal-like gene panel (BLP) consists of *AHNAK2*, *MUC16*, *ITGA3*, and *S100A2* (supplementary material, Figure S6A). We validated these panels by quantifying ISH signals around a punched region ($N = 5$ ROIs/FFPE punch) that was subtyped with NGS [5]. In the pure classical regions there was significantly higher expression of CP and almost no expression of BLP and vice versa (supplementary material, Figure S6A,B). We took advantage of the data from Espinet *et al* [19], which allowed for assessing FACS-purified epithelial cells from PDAC with a known NGS subtype [3]. All genes of the CP were expressed at significantly higher levels in epithelial cells from classical-subtyped tumours, while genes of BLP were expressed higher in those of basal-like-subtyped tumours (supplementary material, Figure S6C). We also assessed the CP and BLP markers from the dataset of Hwang *et al* [20], where 17 PDAC were profiled by single-nucleus RNA sequencing. The original data were reclustered, with the malignant cells selected (16 subclusters in supplementary material, Figure S6D). As an illustration, we highlighted cell clusters where the entire set of CP or BLP were present (supplementary material, Figure S6E). The gene expression dot plot illustrates that clusters expressing all four CP markers were low for the set of BLP markers, and, conversely, clusters that were positive for all BLP markers showed very low to no expression of CP markers. Individual marker gene expression varied considerably (e.g. for *ITGA3*), underscoring the strength of using a panel. These data confirm the specificity of our novel panels for spatially distinguishing the classical and basal-like subtypes. Intra-patient inter-ductal and intra-ductal comparisons showed higher expression of CP markers in *GATA6*^{high} duct (region)s and higher expression of BLP markers in the *GATA6*^{low} duct (region)s (Figure 4A,C and supplementary material, Figure S7A–D). Genes within each panel correlated significantly (Figure 4B,D), although this was more apparent in assessments at the single duct level (Figure 4D).

We also included protein markers of basal-like tumours (i.e. deltaNp63 alias P40, KRT5, and S100A2) used previously as single markers for subtype calling to replace the transcriptomic classification in histological analysis [21–24]. Of these, we found a statistically positive correlation only between S100A2 and *KRAS*^{G12D} (Figure 4B,D). S100A2 is the only protein marker that positively correlated with the BLP, mostly at the single duct level. Tumour ducts display both classical and basal-like regions, with the *GATA6*^{high} ductal part (ROI 1) strongly positive for CP and negative for KRT5 and S100A2. On the *GATA6*^{low} side of the duct (ROI 2, ROI 2'), BLP was highly expressed, and a few KRT5 and S100A2-positive tumour cells could be

observed. Remarkably, P40^{+} cells are present on both sides of the duct and tend to correlate positively with the CP while correlating negatively with the BLP (Figure 4C,D). Individual markers of the panels are shown in supplementary material, Figure S7E. At the single duct level, we measured on average 33% of total

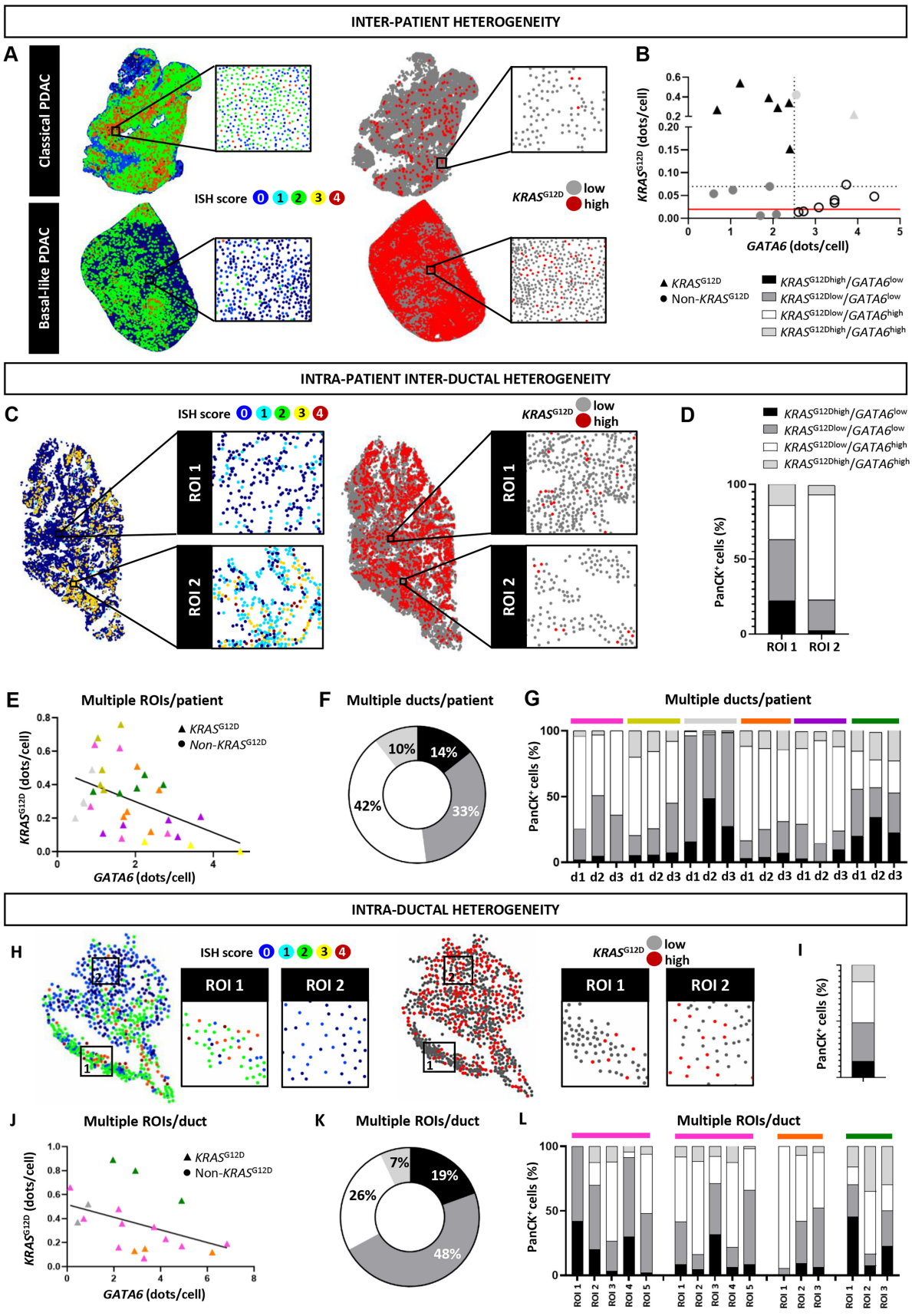

Figure 3 Legend on next page.

ISH signals coming from the CP and 66% from the BLP. The basal protein markers, however, showed little overlap with the BLP, illustrating that the so-called protein markers were missing the majority of the basal-like cells (Figure 4F and supplementary material, Figure S7F). Additionally, some ductal regions co-express CP and BLP markers; three adjacent regions within a single tumour duct exhibited distinct expression patterns, of which the co-expressor cells were located between the CP and BLP regions (Figure 4E). Such 'intermediate' regions (as ROI 2 in supplementary material, Figure S8A) express the CP genes without *GATA6* and the BLP genes without *S100A2*, suggesting that these markers are at the end of the spectra. The individual contribution of our mRNA markers indeed differs from the classical to the intermediate to the basal-like regions, with a main loss of *GATA6*, *EPS8L3*, and *CTSE* (from CP) and a gain of *MUC16* and *ITGA3* (from BLP) (supplementary material, Figure S8B). Interestingly, single-cell measurements of CP and BLP individual markers enabled us to visualise heterogeneity on a subtype scale, pointing to co-expression areas present in all samples (supplementary material, Figure S8D) and suggesting a potential prognostic value of the subtype panels (supplementary material, Figure S8C).

In summary, our novel mRNA marker panels captured the consensus subtypes while basal protein markers that were used previously only detected a minority of cells in the basal-like regions.

Intra-ductal heterogeneity in a functional perspective

To add functional relevance, we plotted the mRNA markers in relation to tumour growth (Ki67) and EMT (co-expression of E-cadherin and vimentin). Interestingly, highly proliferative regions had higher *GATA6* ISH scores (Figure 5A–C). This observation held for all CP markers (Figure 5D,E). Looking at EMT, we observed similar heterogeneity (Figure 5F). Here, ROI 2 illustrates tumour cells with co-localisation for E-cadherin and vimentin that have lower *GATA6*, higher $KRAS^{G12D}$, some S100A2 expression, and increased expression (trend) of the BLP.

We conclude that highly proliferative regions have markers of the classical subtype, while regions with EMT have basal-like markers.

Intra-organoid spatial plasticity is influenced by cancer-associated fibroblasts

We explored whether the intra-ductal heterogeneity was reproduced in organoids. Spatial analysis was performed on patient-derived organoids (PDOs) and compared to PDOs co-cultured with patient-matched cancer-associated fibroblasts (CAFs). Adding CAFs resulted in lower *GATA6* and higher $KRAS^{G12D}$ (Figure 6C,E). When applying the CP or BLP, we could not find significant differences between mono- and co-cultures, except for *GATA6* and *S100A2* (supplementary material, Figure S9A–C,G).

We then compared regions where tumour cells were surrounded by CAFs (CAF-rich, red arrowheads) to tumour regions without CAFs (CAF-poor, white arrowheads). CAF-rich regions had significantly lower *GATA6* and higher $KRAS^{G12D}$ (Figure 6A,B,D,F). Also, CAF-rich regions had lower expression of CP (Figure 6G,H) and higher expression of BLP (Figure 6I,J), and co-expressors in intermediate regions were flanked by regions with high expression of CP or BLP (supplementary material, Figure S9D–F). In the BLP, the contribution of *MUC16* was highly reduced in favour of *ITGA3* and *S100A2* expression in CAF-rich regions (supplementary material, Figure S9H). We did not observe expression of basal-like protein markers in co-cultures (not shown). While there were overall more $Ki67^{+}$ tumour cells present in co- versus monocultures (data not shown), we found less proliferation in CAF-rich versus CAF-poor regions (Figure 6K,L).

Figure 3. Inter-patient, intra-patient inter-ductal, and intra-ductal spatial heterogeneity of *GATA6* and $KRAS^{G12D}$. (A) Whole-section spatial plots of *GATA6* and $KRAS^{G12D}$ expression of classical tumour and of basal-like tumour, according to Chan-Seng-Yue classification [6]. Representative regions are shown as insets. (B) *GATA6* and $KRAS^{G12D}$ ISH quantification on whole-section level, with dotted lines distinguishing four tumour phenotypes. Red line represents BaseScope™ threshold for specificity, excluding four out of 20 patients for further analysis. Mutational status for *KRAS* of individual tumours is indicated. (C) Whole-section spatial plots of *GATA6* and $KRAS^{G12D}$ expression within a single patient. Representative $GATA6^{low}$ region (ROI 1) and $GATA6^{high}$ region (ROI 2) are annotated and shown as spatial plot insets including $KRAS^{G12D}$ detection. (D) Phenotype distribution from panel B in ROI 1 and ROI 2, hence converting these tumour phenotypes into spatial phenotypes. (E) Intra-patient inverse spatial correlation of *GATA6* and $KRAS^{G12D}$, measured on single-cell level in multiple ROIs/patient. $N = 3$–5 ROIs/patient derived from seven different patients, Spearman correlation with $R = -0.46$; two-way ANOVA for repeated measures; $p < 0.0001$. Colour annotation for individual patients as in Figure 1A. Triangles indicate $KRAS^{G12D}$ tumours, confirmed by NGS and/or Idylla. (F) Ring diagram to visualise spatial phenotype distribution between tumour ducts ($N = 3$ ducts/patient derived from six different patients). (G) Spatial phenotype distribution varies in individual tumour ducts within one patient, but not between patients. Colour annotation for individual patients as in Figure 1A. (H) Spatial plots of *GATA6* and $KRAS^{G12D}$ expression within single pancreatic tumour duct. Representative $GATA6^{high}$ region (ROI 1) and $GATA6^{low}$ region (ROI 2) are annotated and shown as spatial plot insets including $KRAS^{G12D}$ detection. Same patient is used as in panels C and D. (I) Spatial phenotype distribution within duct from panel H. (J) Intra-ductal inverse spatial correlation of *GATA6* and $KRAS^{G12D}$, measured on single-cell level in multiple ROIs/duct. $N = 3$–5 ROIs/duct derived from five ducts from four different patients; Spearman correlation with $R = -0.43$; two-way ANOVA for repeated measures; $p = 0.04$. (K) Ring diagram to visualise spatial phenotype distribution within single tumour ducts ($N = 5$ ROIs/duct derived from three different patients). (L) Spatial phenotype distribution varies in different regions of a single tumour duct both between and within patients. Colour annotation for individual patients as in Figure 1A. Triangles indicate $KRAS^{G12D}$ tumours, confirmed by NGS/Idylla.

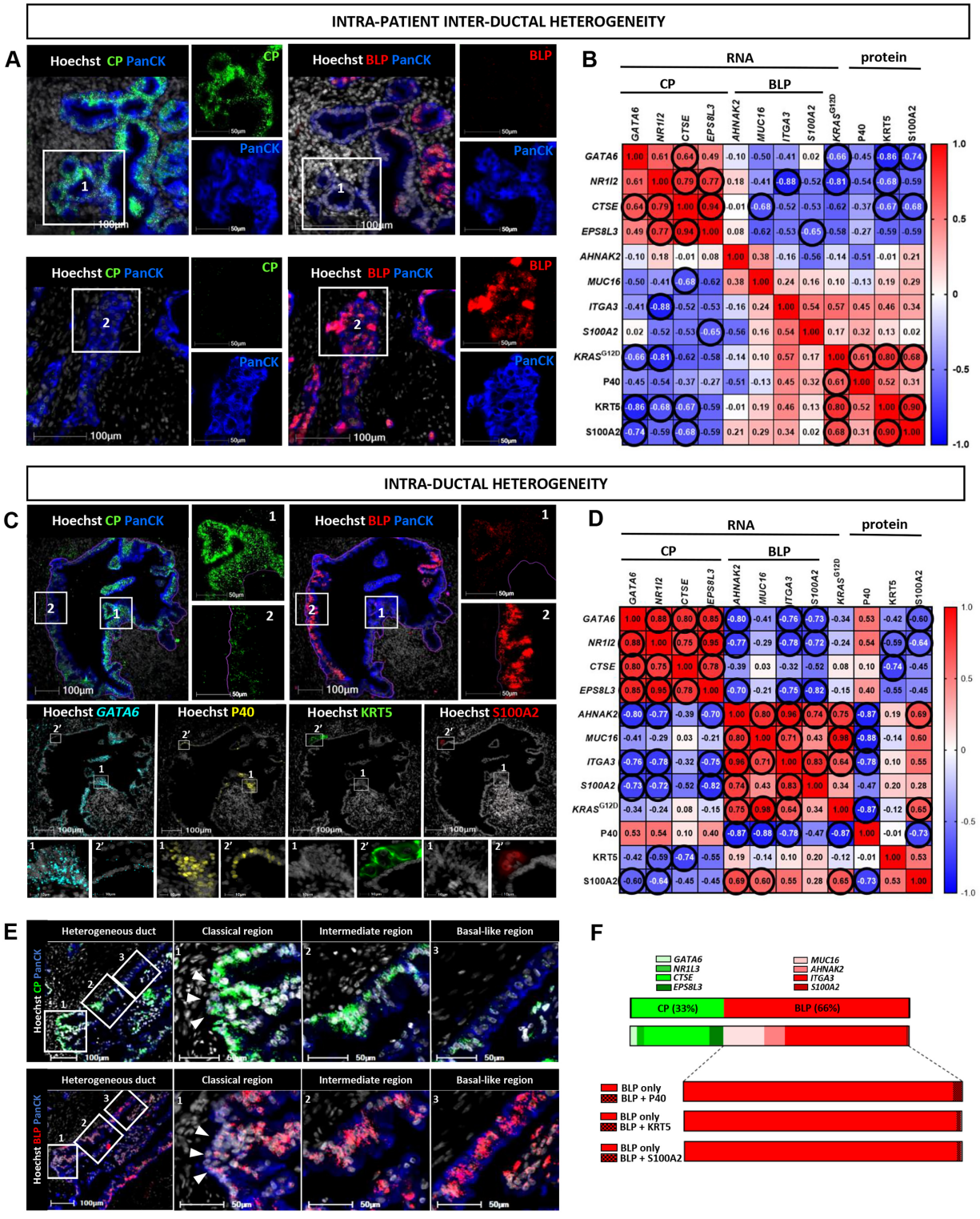

Figure 4. Intra-patient inter-ductal and intra-ductal spatial heterogeneity of a classical and basal-like marker panel. (A) Multiplex RNAScope™ for transcriptomic subtype panels (CP = classical panel; BLP = basal-like panel) on different tumour ducts. (ROI 1, which is *GATA6*^{high}, versus ROI 2, ROI 2', which are *GATA6*^{low}) within a single patient. Scale bars, 100 and 50 µm. (B) Spearman matrix to represent inter-ductal spatial correlations of subtype marker panels and individual genes thereof (RNA detection), *KRAS*^{G12D} detection (RNA), and reported protein markers for basal-like tumours (P40, KRT5, and S100A2). *R* values are shown in matrix. Values are circled when $p < 0.05$. (C) Multiplex RNAScope™ for transcriptomic subtype panels in single tumour duct (CP = classical panel; BLP = basal-like panel) and insets for two ROIs (ROI 1, which is *GATA6*^{high}, versus ROI 2, ROI 2', which are *GATA6*^{low}). Immunofluorescence for basal-like protein markers is shown for this particular duct. Scale bars, 100 and 10 µm. (D) Spearman matrix to represent intra-ductal spatial correlations of subtype marker panels and individual genes thereof (RNA detection), *KRAS*^{G12D} detection (RNA), and reported protein markers for basal-like tumours (P40, KRT5, and S100A2). *R* values are shown in matrix. Values are circled when $p < 0.05$. (E) Multiplex RNAScope™ for transcriptomic subtype panels to visualise continuum present within one duct. Arrowheads = classical region. Scale bars, 100 and 50 µm. (F) Bar plot to visualise subtype panel (CP, BLP) distribution and co-localisation of BLP with basal-like protein markers (P40, KRT5, S100A2) in single tumour ducts ($N = 5$ ROIs/duct in 10 ducts derived from four different patients).

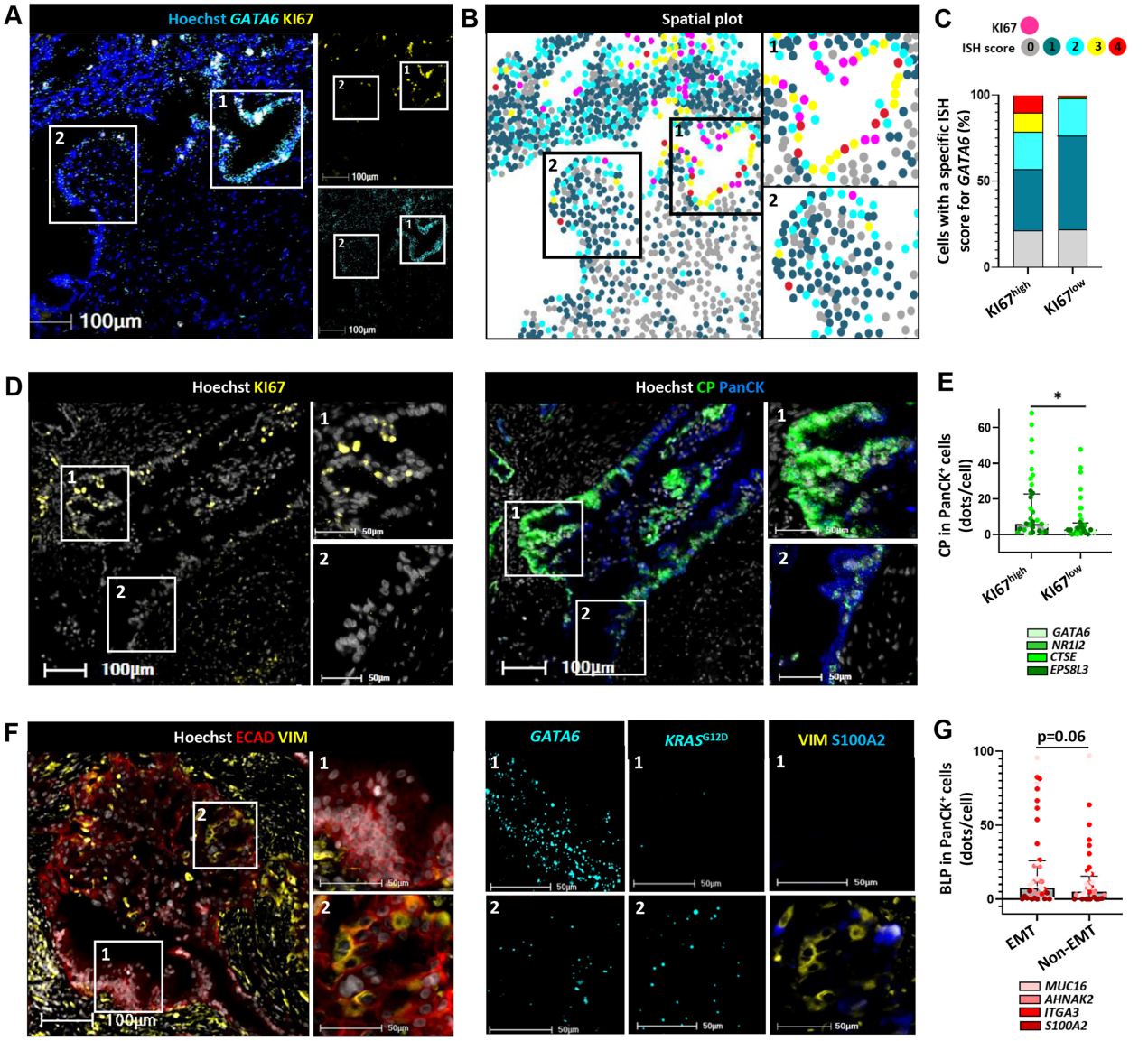

Figure 5. Intra-ductal spatial heterogeneity of functional states. (A) Immunofluorescence for Ki67 and RNAScope™ for *GATA6* within a single tumour duct. Scale bars, 100 µm. (B) Spatial plot with representative KI67^{high} (ROI 1) and KI67^{low} (ROI 2) ductal regions (Ki67^{+} cells in pink) and *GATA6* single-cell expression levels are shown by ISH score (supplementary material, Table S4). (C) Percentage of cells with a certain *GATA6* ISH score in Ki67^{high} versus Ki67^{low} ductal regions. (D) Immunofluorescence for Ki67 and multiplex RNAScope™ for CP within a single tumour duct. Representative Ki67^{high} (ROI 1) and Ki67^{low} (ROI 2) ductal regions are annotated. Scale bars, 100 and 50 µm. (E) CP individual gene quantification of Ki67^{high} versus Ki67^{low} ductal regions. $N = 10$ ROIs/duct in four ducts derived from three different patients; two-way ANOVA for repeated measures; CP: $p = 0.04$; BLP (not shown): $p = 0.56$. (F) RNAScope™, BaseScope™ for *GATA6*, *KRAS*^{G12D} and immunofluorescence for S100A2 within a single tumour duct containing regions with (ROI 2) or without (ROI 1) EMT (co-localisation E-cadherin/vimentin). *GATA6* and *KRAS*^{G12D} are both detected in Cy3 channel. All staining was done on consecutive sections. Scale bars, 100 and 50 µm. (G) BLP individual gene quantification of EMT versus non-EMT ductal regions. $N = 10$ ROIs in four ducts derived from three different patients; two-way ANOVA for repeated measures; CP (not shown): $p = 0.45$; BLP: $p = 0.06$. CP and BLP markers are shown as green and red colour variants respectively.

In conclusion, spatial differences in CAF quantity induce tumour plasticity, with CAF-rich regions having tumour cells with increased *KRAS*^{G12D}, a shift of gene expression in the BLP, and reduced proliferation.

Discussion

Bulk NGS and, more recently, single-cell sequencing, spatial profiling, and AI-based histology have revealed the complexity of human PDAC [2–6,20,24–30], with an emphasis on transcriptomic subtypes and the tumour microenvironment (TME) with different CAF subtypes and immune-suppressive cells. However, we perceived a lack of *in situ* assessment of point mutations (in particular those of *KRAS* that were reported to be amplified in subsets of aggressive patient tumours [3,10,36]) and, beyond *GATA6*, reliable markers that captured the two consensus transcriptomic subtypes *in situ*. Hence, we pursued a single-point mutation RNA-expression analysis and multiplex RNA panels to refine

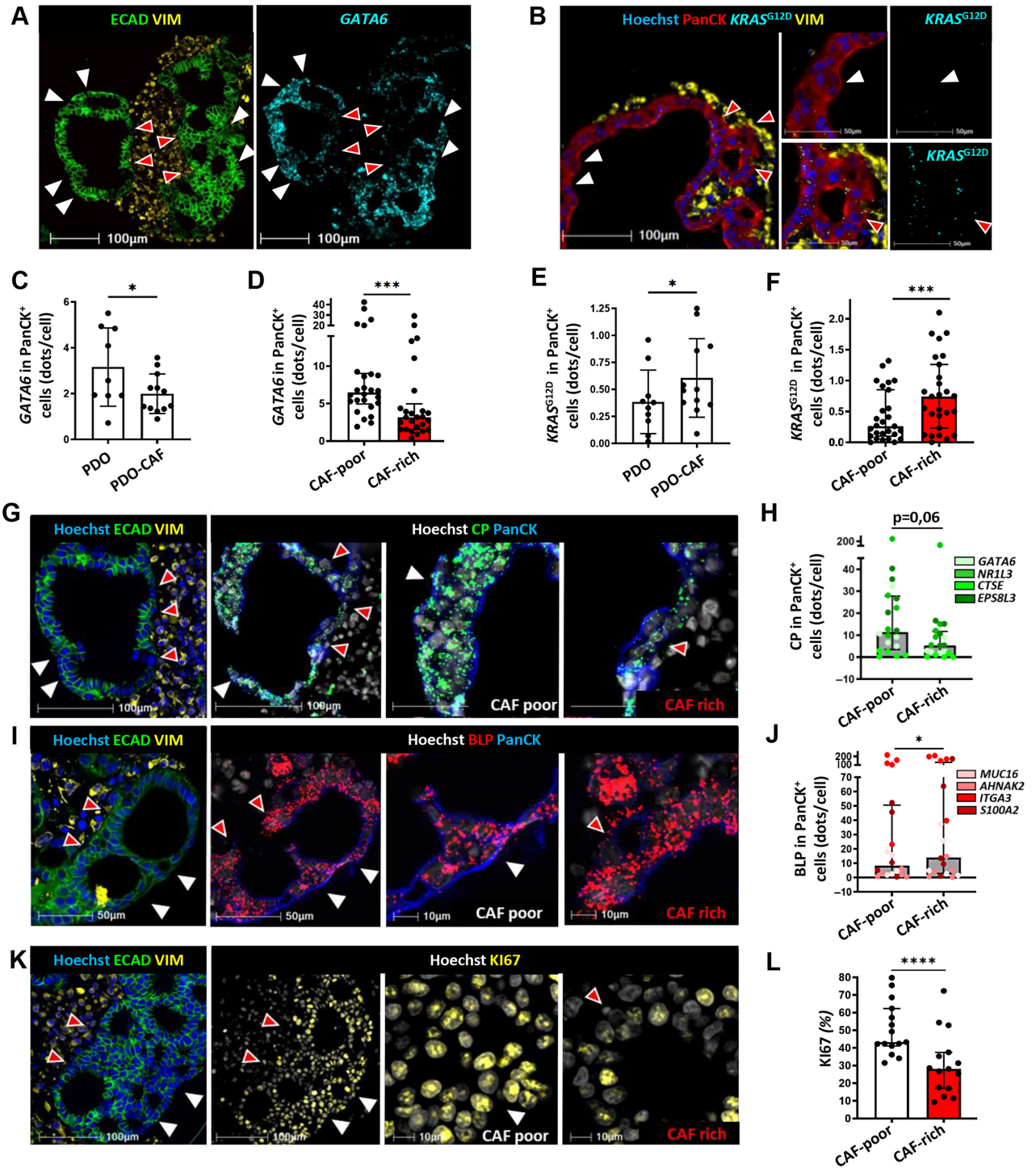

Figure 6. Intra-organoid spatial heterogeneity and plasticity of *GATA6*, *KRAS*^{G12D}, subtype marker panel expression and functional states. (A) Immunostaining for E-cadherin and vimentin in a pancreatic PDO-CAF co-culture. E-cadherin^{+} epithelial cells and vimentin^{+} CAFs indicate CAF-poor (white arrowheads) versus CAF-rich regions (red arrowheads). *GATA6* RNAScope™ in the same PDO as the left panel. Scale bars, 100 µm. (B) Immunostaining for PanCK and vimentin, in addition to *KRAS*^{G12D} (BaseScope™), in a PDO-CAF co-culture. CAF-poor (white arrowheads) versus CAF-rich regions (red arrowheads) are indicated. (C) *GATA6* quantification in monoculture (PDO) versus co-cultures (PDO-CAF). $N = 12$; Wilcoxon; $p = 0.02$. (D) *GATA6* quantification in CAF-poor versus CAF-rich regions. $N = 26$ ROIs from eight different patients; two-way ANOVA for repeated measures; $p = 0.0004$. (E) *KRAS*^{G12D} quantification in monoculture (PDO) versus co-cultures (PDO-CAF). $N = 12$; Wilcoxon; $p = 0.04$. (F) *KRAS*^{G12D} quantification in CAF-poor versus CAF-rich regions. $N = 27$ ROIs from eight different patients; two-way ANOVA for repeated measures; $p = 0.0002$. (G and I) Multiplex RNAScope™ for transcriptomic subtype panels (CP = classical panel; BLP = basal-like panel) in a PDO-CAF co-culture indicating CAF-poor (white arrowheads) versus CAF-rich regions (red arrowheads). Serial section of same organoid as shown in A. (H and J) Quantification of CP and BLP individual genes in PanCK^{+} cells in CAF-poor versus CAF-rich regions. $N = 5$ ROIs from 12 patients; two-way ANOVA for repeated measures; CP: $p = 0.06$; BLP: $p = 0.03$; interaction effect between CAFs and subtype panel with $p = 0.002$ (not shown). CP and BLP markers are shown as green and red variants respectively. (K) Immunostaining for Ki67 in PDO CAF co-culture in CAF-poor versus CAF-rich regions. CAF-poor (white arrowheads) versus CAF-rich regions (red arrowheads) are indicated. Scale bars, 100, 50, and 10 µm. (L) Quantification of Ki67 in CAF-poor versus CAF-rich regions. $N = 16$ ROIs from six different patients; two-way ANOVA for repeated measures; $p < 0.0001$.

our insights into PDAC cell plasticity and heterogeneity at single-cell resolution.

Other than one study of colorectal cancer [16], we are the first to successfully apply BaseScope™ to FFPE samples and for PDAC (cells, tissues, and organoids) we detected *KRAS* mRNA expression *in situ* with high specificity. Although the sensitivity is limited, we identified tumours with $KRAS^{G12D}$ transcripts, which were identified as wild type by NGS. Indeed, applying *in situ* detection overcomes the challenge of low tumour cellularity. *In situ* signal quantification using 3D visualisation, as applied by Molecular Cartography™ (Resolve Biosciences, Monheim am Rhein, Germany), could further improve assay sensitivity. This *in situ* detection of *KRAS* point mutations could be useful for diagnostics and prognostication and is useful in (pre)clinical research, where it allows for distinguishing tumour cells with strong mesenchymal-like characteristics from CAFs in tumour samples.

For pragmatic subtyping in tissue sections, GATA6 protein is the only routinely used staining-based biomarker, including in clinical trial settings [12]. We observed differences in expression of *GATA6*, not only within patients but even up to the level of single pancreatic tumour ducts. We further explored tumour heterogeneity by incorporating $KRAS^{G12D}$ detection, revealing an inverse spatial correlation of *GATA6* and $KRAS^{G12D}$, both between and within tumour ducts, and providing a spatial confirmation of the reported increased gene dosage of *KRAS* in the ($GATA6^{low}$ expressing) aggressive tumours [10,15]. The observation that neighbouring CAFs influence the expression levels of $KRAS^{G12D}$ in the organoid cultures suggests that this might be transcriptionally regulated.

Classifying four spatial phenotypes based on two markers (*GATA6* and $KRAS^{G12D}$) proved a useful exercise to elucidate the strong prevalence of intermediate states that persisted to the highest level of resolution, i.e. single ducts. The observation of intraductal heterogeneity was recently also reported by Williams *et al* [25]. In contrast to that valuable study, we integrated a systematic and quantitative approach with markers directly informed by the transcriptomic signatures from two of the seminal publications of PDAC transcriptomic subtypes [4,5]. Indeed, while *GATA6* as a marker of the classical subtype has been well validated [11,12,31], many studies nowadays use protein markers presumed to reveal the basal-like subtype. We showed that a marker such as deltaNp63/P40 labels only a fraction of basal-like tumour cells. Image analysis even indicated that deltaNp63/P40 showed some positive correlation with the CP. Our staining results underscore that this marker is expressed at the transition of the classical to the basal-like spectrum. This agrees with the mechanistic study from Somerville *et al*, who reported that deltaNp63 was a master regulator of subtype conversion as it reprograms the enhancer landscape to drive squamous transdifferentiation [32]. Once expressed, it binds to enhancers to set off expression of squamous lineage genes (*KRT5*, *S100A2*) but is not necessarily required to maintain it. Indeed, we previously showed that a significant proportion of tumour cell lines that are transcriptomically called basal-like do not express deltaNp63 or only at very low levels. In line with this, deltaNp63 on its own is not a prognostic marker [32]. S100A2 protein, on the other hand, is expressed in vimentin-positive tumour cells, indicative of full EMT. It may be at the final spectrum of the basal-like cell state, as others classified it in metastatic samples (Basal A) [6]. These observations are in agreement with recent publications [25,33], where S100 family proteins are particularly linked to EMT and metastasis [22]. The fact that S100A2 mRNA and protein do not correlate most likely stems from a delayed protein synthesis, as reported during short-term cell adaptation and the process of differentiation state transitioning [34,35], while other transcriptional and translational effects cannot be excluded. Overall, analysis using the CP demonstrated the value of GATA6 as an individual marker. In contrast, analysis using the BLP picks up basal-like tumour cells in their different cell states and discredits currently used 'cherry-picked' basal-like protein markers.

We have here gained important subtype-associated insights by complete dissection and quantification of individual tumour glands in a spatial, functional, and organisational context. We identified tumour populations located on a phenotypic spectrum: on one end, well-differentiated classical tumour cells expressing *GATA6*, and on the other end, undifferentiated mesenchymal-like tumour cells with features of EMT and high-level expression of S100A2 and $KRAS^{G12D}$, in line with the classical-to-basal-like-to-mesenchymal spatio-transcriptomic spectrum, as proposed by Pitter *et al* [25] and Williams *et al* [33]. We added in the proliferative capacity of the tumour cells and underscored the existence of cooperative states, supporting growth by one group and cellular migration and invasion by another group of cells within individual tumour glands [27]. By plotting single-cell mFISH data on a subtype scale, we discovered spatial co-expression of CP and BLP in all samples. In view of Grunwald's findings [24], studies in larger cohorts should assess the extent to which this extensive co-expression relates to survival, as a prognostic value is suggested by our preliminary analysis. Our method is a pragmatic alternative to full transcriptomic profiling, offering a read-out at the single-cell level and in addition spatial assessment of heterogeneity. It can easily be adopted in clinical research and promises more refined insights in subtype changes than the usual single antibody-based biomarker detection.

Raghavan *et al* reported altered transcriptomic profiles of organoids when microenvironmental conditions are changed [25,33]. Here we demonstrated a shift, not only between but also within individual organoids. This was driven by the numbers of surrounding CAFs, further revealing that the degree of plasticity is highly dependent on the spatial context of the TME. We observed only a partial subtype shift from classical to basal-like, suggesting that further manipulation and activation of

CAFs is required, e.g. by other exogenous factors (e.g. transforming growth factor (TGF)-β [22]), and incorporation of other stromal cells might be needed.

The extreme spatial heterogeneity that has become apparent here challenges the use of binary classifications for allocating treatments. Nevertheless, being able to assess the subtype states and their plasticity in a pragmatic way will help to reveal methods to directly steer them, which may ultimately offer prospects for better informed treatment.

Acknowledgements

We are grateful for the service provided by Visual and Spatial Tissue Analysis (https://vsta.research.vub.be). We also thank Lien Willems for her help with quantification and figure design. Funding: Laboratory work in LMMO was supported by Stichting tegen Kanker Translational & Clinical Research Grants 2018 #2092 and by VUB OZR SRP65. IR is a recipient of an Odysseus I fellowship of the Research Foundation-Flanders (G0F8916N). EM was financially supported by Innoser NV and Flanders Innovation & Entrepreneurship (VLAIO).

Author contributions statement

This study was designed and conceptualised by EM, HM, SM and IR. Experiments, spatial analysis, data interpretation and figure design were done by EM, HM, SVL, SM and LELM. NM, RK, PL, ND, LJACH, TA, CB and J-LVL provided human samples. Sequencing analysis was done by PG, CO and RN. EM, HM and IR wrote and edited the manuscript. IR and J-LVL obtained funding for the study.

Data availability statement

Data are available upon reasonable request. All data relevant to the study are included in the article or uploaded as supplementary information. All relevant data can be requested by contacting the corresponding author.

References

1. Siegel RL, Miller KD, Fuchs HE, *et al*. Cancer statistics, 2022. *CA Cancer J Clin* 2022; **72:** 7–33.
2. Collisson EA, Sadanandam A, Olson P, *et al*. Subtypes of pancreatic ductal adenocarcinoma and their differing responses to therapy. *Nat Med* 2011; **17:** 500–503.
3. Moffitt RA, Marayati R, Flate EL, *et al*. Virtual microdissection identifies distinct tumor- and stroma-specific subtypes of pancreatic ductal adenocarcinoma. *Nat Genet* 2015; **47:** 1168–1178.
4. Bailey P, Chang DK, Nones K, *et al*. Genomic analyses identify molecular subtypes of pancreatic cancer. *Nature* 2016; **531:** 47–52.
5. Puleo F, Nicolle R, Blum Y, *et al*. Stratification of pancreatic ductal adenocarcinomas based on tumor and microenvironment features. *Gastroenterology* 2018; **155:** 1999–2013.e3.
6. Chan-Seng-Yue M, Kim JC, Wilson GW, *et al*. Transcription phenotypes of pancreatic cancer are driven by genomic events during tumor evolution. *Nat Genet* 2020; **52:** 231–240.
7. Daemen A, Peterson D, Sahu N, *et al*. Metabolite profiling stratifies pancreatic ductal adenocarcinomas into subtypes with distinct sensitivities to metabolic inhibitors. *Proc Natl Acad Sci U S A* 2015; **112:** E4410–E4417.
8. Wartenberg M, Cibin S, Zlobec I, *et al*. Integrated genomic and immunophenotypic classification of pancreatic cancer reveals three distinct subtypes with prognostic/predictive significance. *Clin Cancer Res* 2018; **24:** 4444–4454.
9. Connor AA, Denroche RE, Jang GH, *et al*. Integration of genomic and transcriptional features in pancreatic cancer reveals increased cell cycle progression in metastases. *Cancer Cell* 2019; **35:** 267–282.e7.
10. Mueller S, Engleitner T, Maresch R, *et al*. Evolutionary routes and KRAS dosage define pancreatic cancer phenotypes. *Nature* 2018; **554:** 62–68.
11. O'Kane GM, Gutiérrez-Sainz L, Ghanem I, *et al*. GATA6 expression distinguishes classical and basal-like subtypes in advanced pancreatic cancer. *Clin Cancer Res* 2020; **26:** 4901–4910.
12. Heredia-Soto V *et al*. The relationship between the expression of GATA4 and GATA6 with the clinical characteristics and prognosis of resectable pancreatic adenocarcinoma. *Biomedicine* 2023; **11:** 252.
13. Juiz N, Elkaoutari A, Bigonnet M, *et al*. Basal-like and classical cells coexist in pancreatic cancer revealed by single-cell analysis on biopsy-derived pancreatic cancer organoids from the classical subtype. *FASEB J* 2020; **34:** 12214–12228.
14. Raghavan S, Winter PS, Navia AW, *et al*. Microenvironment drives cell state, plasticity, and drug response in pancreatic cancer. *Cell* 2021; **184:** 6119–6137.e26.
15. Bournet B, Muscari F, Buscail C, *et al*. KRAS G12D mutation subtype is a prognostic factor for advanced pancreatic adenocarcinoma. *Clin Transl Gastroenterol* 2016; **7:** e157.
16. Baker AM, Huang W, Wang X-MM, *et al*. Robust RNA-based in situ mutation detection delineates colorectal cancer subclonal evolution. *Nat Commun* 2017; **8:** 1998.
17. Wu S, Shi X, Si X, *et al*. EGFR T790M detection in formalin-fixed paraffin-embedded tissues of patients with lung cancer using RNA-based in situ hybridization: a preliminary feasibility study. *Thorac Cancer* 2019; **10:** 1936–1944.
18. Yu S, Shao H, Ban X, *et al*. Detection of POLE subtypes in high-grade endometrioid carcinoma by BaseScope-ISH assay. *Front Oncol* 2019; **9:** 831.
19. Espinet E, Gu Z, Imbusch CD, *et al*. Aggressive PDACs show hypomethylation of repetitive elements and the execution of an intrinsic IFN program linked to a ductal cell of origin. *Cancer Discov* 2021; **11:** 638–659.
20. Hwang WL, Jagadeesh KA, Guo JA, *et al*. Single-nucleus and spatial transcriptome profiling of pancreatic cancer identifies multicellular dynamics associated with neoadjuvant treatment. *Nat Genet* 2022; **54:** 1178–1191.
21. Li H, Jing X, Yu J, *et al*. A combination of cytokeratin 5/6, p63, p40 and MUC5AC are useful for distinguishing squamous cell carcinoma from adenocarcinoma of the cervix. *Diagn Pathol* 2020; **15:** 104.
22. Low RRJ, Fung KY, Gao H, *et al*. S100 family proteins are linked to organoid morphology and EMT in pancreatic cancer. *Cell Death Differ* 2023; **30:** 1155–1165.
23. Haugk B, Horton D, Oppong K, *et al*. Morphological and p40 immunohistochemical analysis of squamous differentiation in endoscopic ultrasound guided fine needle biopsies of pancreatic ductal adenocarcinoma. *Sci Rep* 2021; **11:** 21290.

24. Grünwald BT, Devisme A, Andrieux G, *et al*. Spatially confined sub-tumor microenvironments in pancreatic cancer. *Cell* 2021; **184:** 5577–5592.
25. Williams HL, Costa AD, Zhang J, *et al*. Spatially resolved single-cell assessment of pancreatic cancer expression subtypes reveals co-expressor phenotypes and extensive intratumoral heterogeneity. *Cancer Res* 2022; **83:** 441–445.
26. Karamitopoulou E, Moncada R, Pour M, *et al*. Spatially restricted tumour-associated and host-associated immune drivers correlate with the recurrence sites of pancreatic cancer. *Gut* 2023; **72:** 1523–1533.
27. Barkley D, Moncada R, Pour M, *et al*. Cancer cell states recur across tumor types and form specific interactions with the tumor microenvironment. *Nat Genet* 2022; **54:** 1192–1201.
28. Kalimuthu SN, Wilson GW, Grant RC, *et al*. Morphological classification of pancreatic ductal adenocarcinoma that predicts molecular subtypes and correlates with clinical outcome. *Gut* 2020; **69:** 317–328.
29. Saillard C, Delecourt F, Schmauch B, *et al*. PACpAInt: a deep learning approach to identify molecular subtypes of pancreatic adenocarcinoma on histology slides. *bioRxiv* 2022. https://doi.org/10.1101/2022.01.04.474951. [Not peer reviewed].
30. Martens S, Lefesvre P, Nicolle R, *et al*. Different shades of pancreatic ductal adenocarcinoma, different paths towards precision therapeutic applications. *Ann Oncol* 2019; **30:** 1428–1436.
31. Martinelli P, Pau E C-d S, Cox T, *et al*. GATA6 regulates EMT and tumour dissemination, and is a marker of response to adjuvant chemotherapy in pancreatic cancer. *Gut* 2017; **66:** 1665–1676.
32. Somerville TDD, Xu Y, Miyabayashi K, *et al*. TP63-mediated enhancer reprogramming drives the squamous subtype of pancreatic ductal adenocarcinoma. *Cell Rep* 2018; **25:** 1741–1755.e7.
33. Pitter KL, Grbovic-Huezo O, Joost S, *et al*. Systematic comparison of pancreatic ductal adenocarcinoma models identifies a conserved highly plastic basal cell state. *Cancer Res* 2022; **82:** 3549–3560.
34. Liu Y, Beyer A, Aebersold R. On the dependency of cellular protein levels on mRNA abundance. *Cell* 2016; **165:** 535–550.
35. Natale F, Vivo M, Falco G, *et al*. Deciphering DNA methylation signatures of pancreatic cancer and pancreatitis. *Clin Epigenetics* 2019; **11:** 132.
36. Buscail L, Bournet B, Cordelier P. Role of oncogenic KRAS in the diagnosis, prognosis and treatment of pancreatic cancer. *Nat Rev Gastroenterol Hepatol* 2020; **17:** 153–168.
37. Broutier L, Andersson-Rolf A, Hindley CJ, *et al*. Culture and establishment of self-renewing human and mouse adult liver and pancreas 3D organoids and their genetic manipulation. *Nat Protoc* 2016; **11:** 172443.
38. Pinto MP, Jacobsen BM, Horwitz KB. An immunohistochemical method to study breast cancer cell subpopulations and their growth regulation by hormones in threedimensional cultures. *Front Endocrinol* 2011; **2:** 15.

References 37 and 38 are cited only in the supplementary material.

SUPPLEMENTARY MATERIAL ONLINE

Supplementary materials and methods

Figure S1. Inter-patient, intra-patient inter-ductal, and intra-ductal heterogeneity of *GATA6* expression

Figure S2. Spatial plots of *GATA6* on whole tissue sections of whole PDAC cohort

Figure S3. Spatial plots of *GATA6* in single tumour ducts of human PDAC cohort

Figure S4. BaseScope™ reliably detects *KRAS*-specific point mutations in PDAC cell lines

Figure S5. Inter-patient, intra-patient inter-ductal, and intra-ductal spatial heterogeneity of *GATA6* and $KRAS^{G12D}$

Figure S6. Validation of classical and basal-like marker panel using multiplex RNAScope™

Figure S7. Intra-patient inter-ductal and intra-ductal spatial heterogeneity of a classical and basal-like marker panel

Figure S8. Intra-ductal spatial heterogeneity of classical and basal-like marker panel

Figure S9. Intra-organoid plasticity is influenced by cancer-associated fibroblasts

Table S1. BaseScope™ and RNAScope™ probes used

Table S2. Antibodies used for immunostaining

Table S3. Individual patient data and tumour characteristics

Table S4. Semi-quantitative scoring system for RNAScope™

Table S5. Clinicopathological variables of whole cohort